Impact of Temperature and Doping on the Performance of Ge/Ge$_{1-x}$Sn$_x$/Ge Heterojunction Phototransistors
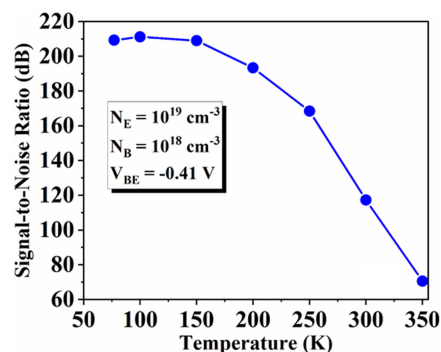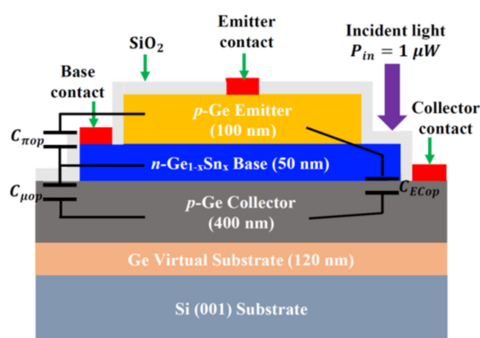
Harshvardhan Kumar
Rikmantra Basu, *Member, IEEE*
Guo-En Chang, *Member, IEEE*

Impact of Temperature and Doping on the Performance of Ge/Ge$_{1-x}$Sn$_x$/Ge Heterojunction Phototransistors

Harshvardhan Kumar [ID]**,**[1] **Rikmantra Basu,**[1] *Member, IEEE,*
and Guo-En Chang [ID]**,**[2] *Member, IEEE*

[1]Electronics and Communication Engineering Department, National Institute of Technology
Delhi, Institutional Area, IAMR Campus, New Delhi 110040, India
[2]Department of Mechanical Engineering and Advanced Institute of Manufacturing with
High-Tech Innovations, National Chung Cheng University, Chiayi County 62102, Taiwan

Abstract: We study the effect of temperature and doping in Si-based GeSn heterojunction phototransistors (HPTs) for low-power-consuming, low-cost, and high-speed mid-infrared (MIR) applications. The incorporation of Ge$_{1-x}$Sn$_x$ alloy in the base of our HPTs significantly shortens the emitter-to-collector transit time, leading to high cut-off frequency (f_T) due to an increase in mobility. Furthermore, the Ge$_{1-x}$Sn$_x$ base extends the optical detection over a wide range (up to 2500 nm) due to the shrinkage of the bandgap energy caused by alloying with Sn. Additionally, spectral responsivity increases with Sn alloying due to the increased absorption coefficient. Our results show that f_T and responsivity are strongly dependent not only on doping but also on temperature. The impact of temperature on the noise behavior of phototransistors was also analyzed for frequencies up to 100 GHz. As the temperature increased, the signal-to-noise ratio (SNR) decreased; however, spectral responsivity significantly improved. The high SNR, responsivity, and f_T values of the GeSn HPT make it a potential candidate for future Si-based uncooled high-speed MIR photodetection.

Index Terms: Cut-off frequency, doping, GeSn alloy, heterojunction phototransistor (HPT), responsivity, temperature, transit time.

1. Introduction

Photodetectors (PDs) responding to the mid-infrared (MIR) wavelength range (2–3 μm) have broad applications, including blood glucose sensing, molecular spectroscopy, remote-trace gas sensing, radiation thermometry, laser radar systems, and high-temperature ultraviolet photodetection [1], [2]. PDs with low noise, high internal gain, low response time, and high spectral responsivity (SR) in the MIR range are of great interest because they have high fan-out capacity and lower requirements for additional electronic circuitry. Among the various types of PDs, heterojunction phototransistors

(HPTs) have particularly attracted attention because they provide an extremely high gain [3], high signal-to-noise ratio (SNR) [4], and high responsivity [5] without the excess noise that characterizes avalanche photodetectors (APDs) [6].

Several III-V compound MIR PDs and HPTs have been studied in both low-temperature and high-temperature sensing applications [3], [5]–[8]. They manifest maturity problems, such as integration incompatibility, high toxicity, and low thermal conductivity, which is unlike Si [9], and relatively high cost. Recently, attention has shifted to all-group-IV approaches to address the above-mentioned problems. However, Si has a cut-off wavelength ($\lambda_{cut-off}$) of 1100 nm (corresponding to a frequency of 272.7 THz) and a low absorption coefficient, due to its indirect bandgap characteristic. Thus, Si PDs are not suitable for C-band or L-band fiber-optic telecommunication or MIR photodetection. Conversely, Ge has a relatively low direct bandgap of 0.8 eV, which leads to $\lambda_{cut-off}$ of 1550 nm. Thus, Ge PDs are suitable candidates for C-band telecom applications. However, because it is still difficult to attain effective photodetection in the L-band and beyond, they are unsuitable for longer wavelength applications.

GeSn alloys are potential candidates for MIR photodetection in various applications [10]. The unique advantages of complementary metal-oxide-semiconductor (CMOS) compatibility, high electron and hole mobility (μ_p) [11]–[17], larger absorption spectra [18], and the direct nature of bandgap for bulk GeSn with an Sn content >6% make GeSn alloys [19], [20] attractive candidates for MIR applications. Despite the limited solid solubility of Sn in Ge, $Ge_{1-x}Sn_x$ alloys with Sn concentrations up to 28% have been grown on an Si substrate using low-temperature growth techniques, such as molecular beam epitaxy, chemical vapor deposition (CVD) [21], and sputtering epitaxy [22] techniques. Recently, APDs and p-i-n PDs based on the GeSn alloy have also been studied [23]–[26]. The application of GeSn alloys in HPTs for fiber-optic telecommunication networks and MIR applications has been theoretically studied in recent works [27]–[30]. Recently, a two-terminal *n-p-n* GeSn HPT on Ge with Sn concentrations of 6.5% was fabricated for operation at 1550 nm and 2003 nm, which had an SR 10 times higher than conventional GeSn-based PDs [31]. Floating *p-n-p* GeSn HPTs on Si have also been recently demonstrated with an extended photodetection range up to 1940 *nm* and enhanced optical responsivity [32]. In addition, the proper selection of Sn concentrations in GeSn alloys causes a redshift in the cut-off wavelength because bandgap energy decreases with increasing Sn concentrations. Another potential advantage of using GeSn-based HPTs is that they have a high SNR [28] and low-voltage of operation compared to conventional III-V compound based PDs [33] and HPTs [34]. Therefore, GeSn-based HPTs are a viable alternative to conventional PDs for attaining high SR and a wide range of photodetection.

For MIR PDs, noise is a significant problem. It is strongly influenced by the operation temperature. The performance of HPTs depends heavily on various parameters, such as temperature and doping-dependency. For example, capacitance, base and the emitter resistance, base transport factor, and injection efficiency strongly depend on the emitter and base doping concentrations and the operating temperature. Therefore, the sensitivity, spectral response, frequency, and noise performance are significantly influenced by the operating temperature and doping levels of the device. Thus, it is crucial to analyze the temperature- and doping-dependent performance of GeSn-based *p-n-p* HPTs to achieve high-performance photodetection. In this work, our objective is to theoretically investigate the performance of three-terminal (3-T) *p-n-p* GeSn HPTs in a common-emitter (C-E) configuration. We aim to determine the impact of doping and temperature on SR, various noise components, SNR, absorption coefficient, transit time, and the frequency performance of MIR GeSn HPTs. We also aim to study the effect of Sn concentrations in the active $Ge_{1-x}Sn_x$ layer (base layer) and the various structural parameters, to optimize the structure for maximizing the frequency performance and SR.

The remainder of this paper is organized as follows. Section II shows the HPT structure and layer parameters. Section III explains the theoretical models. The impact of doping and temperature on the frequency performance and SR of HPTs are explained in Section IV. Finally, our conclusions are presented in Section V.
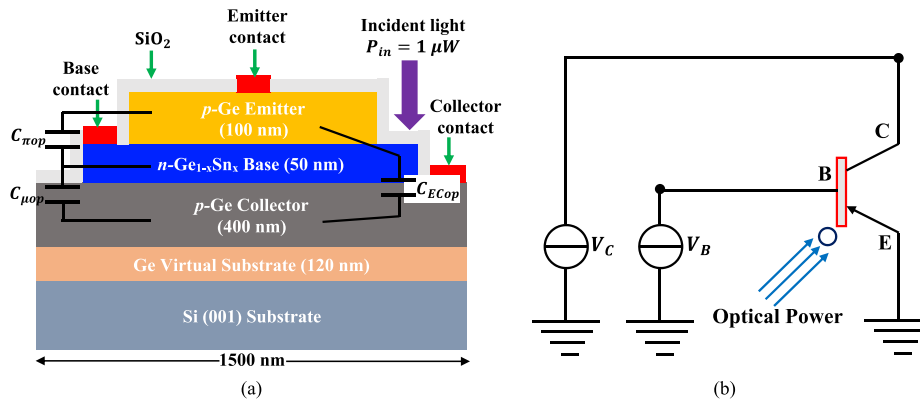
Fig. 1. (a) Layered structure and (b) schematic of 3-terminals of our designed normal-incident *p-n-p* Ge/Ge$_{1-x}$Sn$_x$/Ge HPTs on silicon.

TABLE 1
Structural Details of Our Designed Ge$_{1-x}$Sn$_x$/Ge HPTs

Layer	Material	Thickness t (nm)	Doping Level (cm^{-3})	Type
Emitter	Ge	100	1×10^{19}	p
Base	Ge$_{1-x}$Sn$_x$	50	1×10^{18}	n
Collector	Ge	400	1×10^{17}	p
Virtual substrate	Ge	120	-	i
Substrate	Si	-	-	i

2. Device Structure

The GeSn HPT used in this study has three terminals, a named base (B), a collector (C), and an emitter (E), implemented in a C-E configuration (Fig. 1). The material, layer thickness, and doping density of each epilayer are given in Table 1. The widths of the emitter, base, and collector are 900 nm, 1200 nm, and 1500 nm, respectively. The optical signal of power 1μW is incident normally at the emitter-base heterointerface. The device structure consists of the Ge virtual substrate (VS) with a thickness of 120 nm to reduce the defects during epitaxy on the Si (001) substrate [30]. The GeSn base layer is 50-nm thick, less than the critical thickness [35]; thus, the entire HPT stack is pseudomorphic regarding the underlying Ge VS. Therefore, the Ge layers are strain-free, and the Ge$_{1-x}$Sn$_x$ layer is subjected to a compressive strain of $\varepsilon = -0.143x$ [36]. Here, we consider Ge$_{1-x}$Sn$_x$ alloys with two moderate Sn concentrations: 6% and 9%, which allows for effective MIR photodetection. The Ge$_{1-x}$Sn$_x$base layer can enhance the absorption coefficient to yield high responsivity in the MIR wavelength region. The device design consists of doping concentrations of 1×10^{19} cm^{-3}, 1×10^{18} cm^{-3}, and 1×10^{17}cm^{-3} for the emitter, base layer, and collector layer, respectively.

3. Theoretical Models

In this section, we present our theoretical models to calculate the 3-dB cut-off frequency (f_T), maximum frequency ($f_{\max}$), capacitance, base resistance, various noise components, and SNR. The optical absorption coefficient for the designed Ge$_{1-x}$Sn$_x$/Ge HPT is taken from [19] and [21]. The temperature-dependent μ_p and direct bandgap energy of Ge are taken from [35] and [36]. The

saturation velocity of $Ge_{1-x}Sn_x$ is not yet available; thus, it is assumed to be the same as that of pure Ge [39]. The band structures of GeSn/Ge heterostructures are calculated using the deformation potential theory, and the optical absorption coefficient is calculated using Fermi's golden rule. The models with responsivity are available in [21], and the parameters of GeSn are reported in [12] and [21].

3.1 Frequency Performance of HPT

The frequency performance of HPT is characterized by the 3-dB f_T (f_T represents the theoretical highest speed that an HPT can give), f_{max} (f_{max} represents the maximum operating frequency at which an HPT can operate), and transit time. Doping concentration and operating temperature play a crucial role in maintaining satisfactory performance of high-speed and low-noise PDs. Thus, the selection of an optimal doping concentration in the emitter and base layers are fundamental steps for designing high-speed HPTs. The impact of doping and temperature on frequency performance, RC time constant (τ_{RC}), and forward transit time delay (τ_F) can be evaluated using f_T and f_{max} [40].

$$f_T = \frac{1}{2\pi \tau_{Total}} = \frac{1}{2\pi \left[r_e C_{ECop} + \tau_F \right]} = \frac{1}{2\pi \left[\left(\frac{kT}{qI_{Eop}} \right) C_{ECop} + \tau_b + \tau_{bc} \right]} \tag{1}$$

$$f_{max} = \sqrt{\frac{1}{(2\pi \tau_{Total}) 8\pi C_{\mu op} R_{Bop}}} = \sqrt{\frac{f_T}{8\pi C_{\mu op} R_{Bop}}}, \tag{2}$$

where τ_{Total} is the total time delay for carriers transiting from the emitter layer to the collector layer; r_e is the small-signal emitter resistance, and C_{ECop} is the total capacitance (which consists of base-emitter junction capacitance, $C_{\pi op}$, and base-collector junction capacitance, $C_{\mu op}$). k is the Boltzmann constant; T is the temperature in K; q is the electronic charge, and I_{Eop} is the emitter current under illumination. τ_b and τ_{bc} are the base transit time and base-collector transit time delay, respectively, and R_{Bop} is the base resistance under illumination. The doping-dependent base resistance and capacitance can be calculated using (3)–(5) [40].

$$R_{Bop} = \frac{1}{2L_E} \left(\frac{S_E}{6t_B q N_B \mu_n} + \rho_{bsop} S_{EB} + \rho'_{bsop} L_T \cot \left(\frac{S_B}{L_T} \right) \right), \tag{3}$$

$$C_{\pi op} = \frac{\epsilon_E A_E}{t_{BEop}} + \left[\frac{t_B^2}{2D_{pb}} + \frac{t_B}{v_s} + \frac{t_{BCop}}{2v_s} \right] g_{mop}, \tag{4}$$

$$C_{\mu op} = \frac{L_E \epsilon_c}{t_{BCop}} \left(S_E + 2S_{EB} + 2S_B \right), \tag{5}$$

where ρ_{bsop} and ρ'_{bsop} are the sheet resistance of the extrinsic base layer between the emitter layer and the base contact and that of the base layer, respectively. S_E, S_B, and S_{EB} are the width of the emitter, base stripe, and the emitter-base separation, respectively. L_E is the width of the device; t_B is the thickness of the base layer; N_B is the base doping, and μ_n is the electron mobility. ϵ_E, ϵ_c, and v_s are the permittivity of the emitter, permittivity of the collector, and saturation velocity, respectively; A_E, D_{pb}, and t_{BCop} represent the cross-sectional emitter area, hole diffusion constant (D_p), and the base-collector depletion region under illumination, respectively. g_{mop} and t_{BEop} are the transconductance and the base-emitter depletion region under illumination, respectively.

3.2 Noise Components and SNR

The advantage of HPTs is their low noise and high SNR compared to conventional APDs. The SNR at the output of the HPTs depends significantly on the voltage gain (A_v) and the transfer function of the equivalent circuit model of the HPT [41] and can be defined as the ratio of average output signal power to the average mean square value of the total noise current. In general, an HPT comprises four major noise components, including Johnson-Nyquist (thermal) noise (N_3), $1/f$ noise, shot noise

current component at the B-E junction (N_2), and shot noise current component at the B-C junction (N_1). However, $1/f$ noise exists only below 1 MHz; therefore, this noise component is not considered in the present study. A_v and transfer function are expressed as follows [41]:

$$A_V(s) = \frac{-g_{mop} + sC_{\mu op}}{\frac{1}{R_i} + sC_{\mu op}},$$ (6)

$$H(s) = \frac{g_{mop}\left(s + \frac{1}{R_i c_{\mu op}}\right)}{s^2 C_{\pi\,op} + \left(\frac{C_{\pi\,op}}{R_i C_{\mu op}} + \frac{1}{R_i} + g_{mop} + g_{\pi\,op}\right)s + \frac{g_{\pi\,op}}{R_i C_{\mu op}}}$$ (7)

where R_i is the input resistance; $g_{\pi\,op}$ is the input conductance in illumination, and s represents the Laplace domain parameter ($s = j\omega = j2\pi f$). The SNR of HPTs can be defined as

$$SNR = \frac{S_{out}}{N_{out}} = \frac{i_{ph}^2\left(|H(s)|^2\right)R_{eq}}{\left(i_n^2(s)\right)R_{eq}} = \frac{i_{ph}^2\left(|H(s)|^2\right)}{\left(i_n^2(s)\right)},$$ (8)

where $i_n^2(s)$ is the average mean square value of the total noise current and can be broken into three components: Johnson-Nyquist noise, shot noise across the B-E junction, and shot noise across the B-C junction. The expressions for noise components are standard and are taken from [41].

$$N_1 = \frac{1}{\beta^2}\left(1 - \frac{C_{\pi\,op}^2}{g_{\pi\,op}^2}s^2\right)\overline{i_{2op}^2}|H(s)|^2 + \frac{R_{bop}^2}{\beta^2}\left(1 - \frac{C_{\pi\,op}^2}{g_{\pi\,op}^2}s^2\right)\overline{i_{2op}^2}g_{mop}^2$$

$$+ \frac{1}{\beta^2 g_{\pi\,op}}\left(\frac{1}{g_{\pi\,op}} + 2R_{bop}\right)\overline{i_{2op}^2}g_{mop}^2 + 2|H(s)|^2\frac{1}{\beta^2}$$

$$\times\left[R_{bop}\left(1 - \frac{C_{\pi\,op}^2}{g_{\pi\,op}^2}s^2\right)\overline{i_{2op}^2} + \frac{\overline{i_{2op}^2}}{g_{\pi\,op}}\right](g_{\pi\,op} + j2sC_{\mu op}A_{vi})$$

$$+ 2|H(s)|^2\left[-\frac{C_{\pi\,op}\overline{i_{2op}^2}}{\beta^2 g_{\pi\,op}^2}s^2\{C_{\pi\,op} + C_{\mu op}(1 - A_{vr})\}\right]$$ (9)

$$N_2 = \overline{i_{1op}^2}|H(s)|^2 + R_{bop}^2\overline{i_{1op}^2}g_{mop}^2 + 2\overline{i_{1op}^2}R_{bop}g_{\pi\,op}|H(s)|^2,$$ (10)

$$N_3 = \overline{v_{rop}^2}g_{mop}^2,$$ (11)

where β is the current gain; $\overline{i_{1op}^2}$ and $\overline{i_{2op}^2}$ represent the mean square value of the shot noise current computed across the B-E and B-C junctions under illumination, respectively, and A_{vr} and A_{vi} represent the real and imaginary parts of A_v, respectively. $\overline{v_{rop}^2}$ represents the mean thermal noise square voltage.

3.3 Temperature-dependent Bandgap Energy, Mobility, and Diffusion Constant

In this work, we considered the temperature-dependent bandgap energy of Ge, μ_p, and hole D_p to compute the temperature-dependent capacitance and emitter resistance, and their impact on the transit time, f_T, and SNR of our designed HPT. The temperature-dependent bandgap energy, mobility, and D_p are expressed as follows [37], [38].

$$E_G(T) = E_G(0) - \frac{5.82 \times 10^4 \times T^2}{T + 296}$$ (12)

$$\mu_p(T) = 1.05 \times 10^4 \times \left(T^{-2.33}\right)$$ (13)

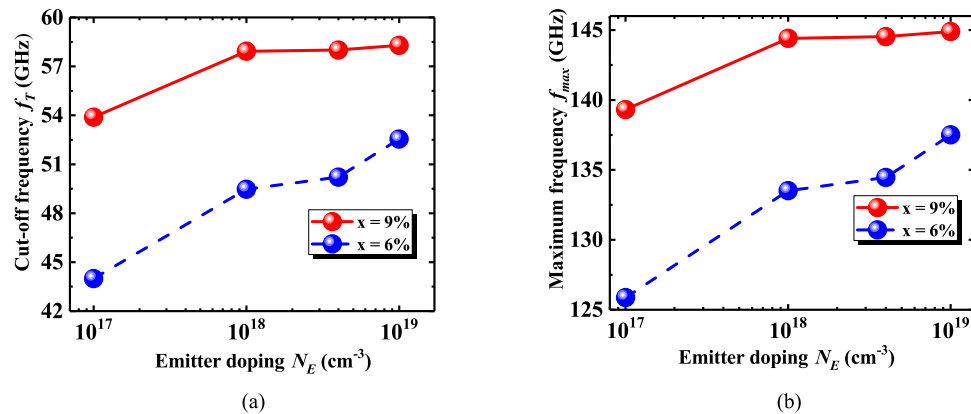$$D_p(T) = \frac{kT}{q} \times 1.05 \times 10^4 \times \left(T^{-2.33}\right) = V_T(T) \times \mu_p(T),$$ (14)

Fig. 2. Calculated (a) f_T, and (b) f_{max} with emitter doping concentrations for two Sn compositions in the $Ge_{1-x}Sn_x$ base with different Sn contents.

where $E_G(T)$ is the temperature-dependent bandgap energy in eV; $E_G(0)$ stands for the bandgap energy in eV at 0 K, and T is the temperature. $\mu_p(T)$ is the temperature-dependent μ_p in m^2/Vs and $D_p(T)$ is the temperature-dependent diffusion constant in m^2/s.

4. Results and Discussion

In this section, the effect of emitter and base-layer doping concentrations, operating temperature, and collector current on the performance of GeSn HPTs are presented through the evaluation of the f_T, f_{max}, SR, various noise spectra, and SNR.

4.1 Impact of Emitter Doping Concentrations on Frequency Performance and Spectral Responsivity

We first discuss the impact of the emitter doping level on frequency. Fig. 2 shows the variations in the f_T and f_{max} of HPT as a function of the emitter doping concentration for the fixed-base-layer doping concentration (N_B) of $1 \times 10^{18} cm^{-3}$. Both f_T and f_{max} increase with emitter doping concentration. This behavior can be explained by the emitter transit time delay (RC time delay), which decreases with emitter doping concentration (2.6 ps $\sim$ 2 ps for $x = 6\%$ and 1.98 ps $\sim$ 1.75 ps for $x = 9\%$). However, the τ_F (which consists of both base transit time (τ_b) and base-collector transit time (τ_{bc})) is independent of the emitter doping concentration. Therefore, f_T and f_{max} are functions of the emitter doping concentration and are significantly influenced by the emitter transit time delay. Fig. 2 also shows that f_T and f_{max} increase with increasing Sn composition in the $Ge_{1-x}Sn_x$ base (from $x = 6\%$ to $x = 9\%$, f_T increases by $\sim$ 11% and f_{max} increases by $\sim$ 5.4% for an emitter doping concentration (N_E) of $1 \times 10^{19} cm^{-3}$). The increases in frequency are attributed to the increase in mobility with increasing Sn concentrations [12]. Furthermore, from Fig. 2, as Sn concentration increases to 9%, f_T and f_{max} initially increase with doping in the emitter layer at $N_E = 10^{17} cm^{-3}$ to $10^{18} cm^{-3}$, but then they become almost constant for doping concentrations of $N_E = 10^{18} cm^{-3}$ to $10^{19} cm^{-3}$.

Next, we discuss the impact of the emitter doping level on SR for a fixed-base-layer doping concentration of (N_B) of $1 \times 10^{18} cm^{-3}$. Fig. 3 shows the calculated SR as a function of emitter doping concentration for an Sn concentration of 9% at different wavelengths. The results show that SR slightly increases with emitter doping concentrations. Because responsivity is strongly dependent on the current gain (SR $\propto$ gain), with an increase in emitter doping concentrations, the current gain increases [42], leading to an increase in responsivity. However, a heavily doped emitter will cause a high-tunneling current across the junction, leading to degradation of direct
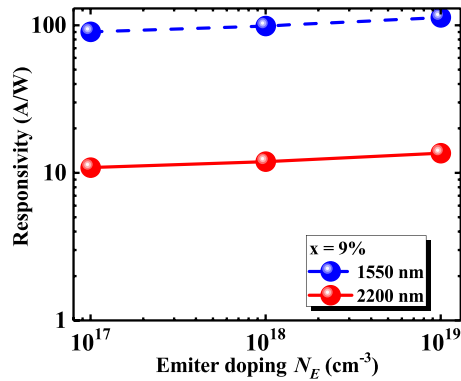
Fig. 3. Calculated SR as a function of emitter doping concentration for x = 9% at two different wavelengths, λ = 1550 nm and 2200 nm.
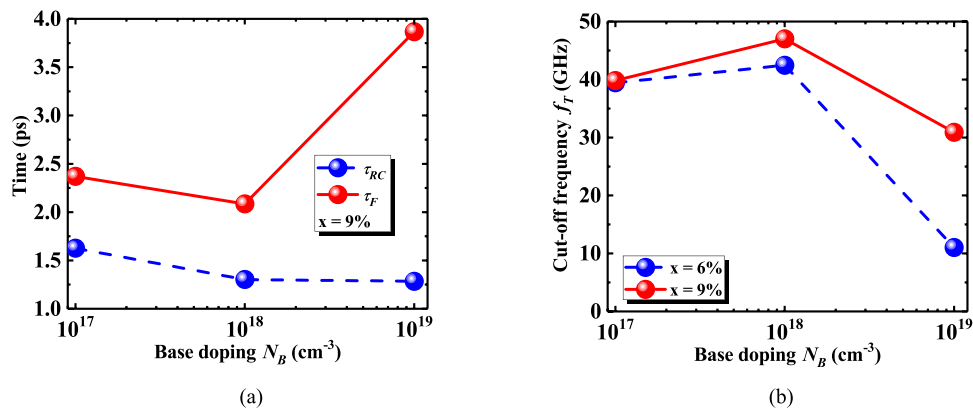

Fig. 4. Variations of (a) time delay, and (b) f_T with base doping concentration.

current performance. Therefore, optimization of doping in the emitter layer is crucial to balance these effects. Therefore, $N_E = 1 \times 10^{19} \text{cm}^{-3}$ was determined to be optimal in this work.

4.2 Impact of Base Doping Concentration on Frequency Performance and Spectral Responsivity

In this section, we study the effect of base doping concentrations on f_T, time delay, and SR for a fixed emitter doping concentration of $N_E = 1 \times 10^{19} \text{cm}^{-3}$. Fig. 4 shows the variations of RC time delay and the τ_F and f_T with base-layer doping concentrations. The calculated result shows that base doping concentration has a significant impact on the forward transit time and has less impact on the RC time delay (RC time delay decreases with increasing doping concentration in the base layer). Hence, the forward transit time has a great impact on the variation of f_T with base doping concentration (shown in fig. 4(b)). As shown in fig. 4(a), forward transit time decreases first, attains its minimum value at a base doping concentration of $1 \times 10^{18} \text{cm}^{-3}$, and then increases with higher base doping concentrations. This is because the base layer is heavily n-doped. As the doping concentration in the base layer increases, the majority of charge carriers (electrons) will have a high rate of ionized impurity scattering [43]. Hence, there will be a large amount of electrons in fast relaxation motion, which is useful to realize the holes as a uni-traveling carrier to reduce the negative impact of electron mobility, and this results in reducing the hole transit time required for the photogenerated electrons to drift across the base-emitter (B-E) junction heterointerface
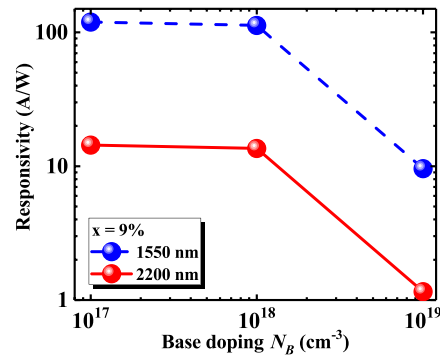
Fig. 5. Calculated responsivity as a function of base doping concentration for x = 9% at two different wavelengths, λ = 1550 nm and 2200 nm.
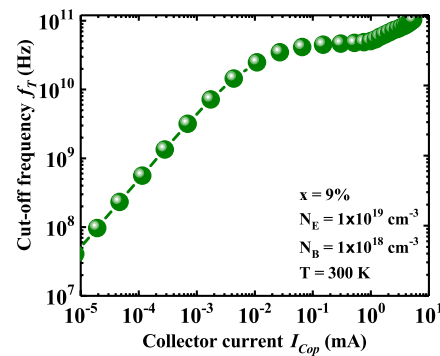

Fig. 6. f_T versus collector current for Sn concentration of 9%.

[43]. At the same time, the hole diffusion constant (D_p) decreases lead to an increase in the forward transit time. For lower base doping concentration, the fast relaxation rate of the electrons causes an increase in f_T irrespective of the decrease caused by the hole transit time. Therefore, f_T increases first and attains a peak value at a base doping concentration of $1 \times 10^{18} \mathrm{cm}^{-3}$. A further increase in base doping concentration causes a decrease in f_T. This is because the high base doping concentration has a great impact on the hole transit time (an increase in base doping concentration decreases the hole mobility and hole diffusion constant (D_p); therefore, forward transit time increases), which in turn decreases the f_T of the device. The result shows that the minimum time delay is obtained at a base doping concentration N_B of $1 \times 10^{18} \mathrm{cm}^{-3}$. Therefore, the maximum f_T of $\sim$ 50 GHz (x = 9%) is also attained at a base doping concentration of $1 \times 10^{18} \mathrm{cm}^{-3}$.

Fig. 5 shows the impact of the base doping concentration on SR for the Sn concentration of 9% at different wavelengths. With an increase in base doping concentrations, responsivity decreases significantly. With high base doping, the base-collector depletion region shrinks, and impurity scattering reduces the minority carrier lifetime and hole diffusion length. Therefore, a low base doping concentration is preferred to achieve a high SR, but to attain high-frequency operation, high base-layer doping is required to decrease the base resistance (Eq. 2). Therefore, $N_B = 1 \times 10^{18} \mathrm{cm}^{-3}$ was determined to be optimal in this study for obtaining high responsivity and high-frequency operation in our designed HPT.

4.3 Impact of Collector Current on the Cut-off Frequency

Fig. 6 represents the variations in the f_T with the collector current for the fixed emitter and base layer doping concentrations of $N_E = 1 \times 10^{19} \mathrm{cm}^{-3}$ and N_B of $1 \times 10^{18} \mathrm{cm}^{-3}$, respectively. The results
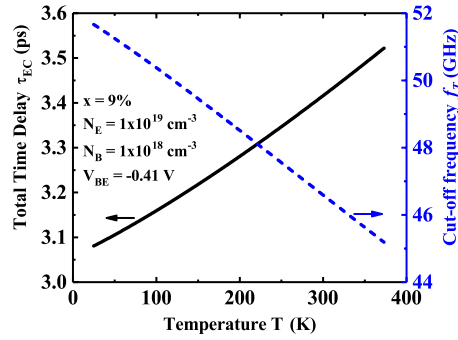
Fig. 7. Calculated total time delay (emitter-to-collector) and f_T as a function of temperature for Sn concentration of 9%.
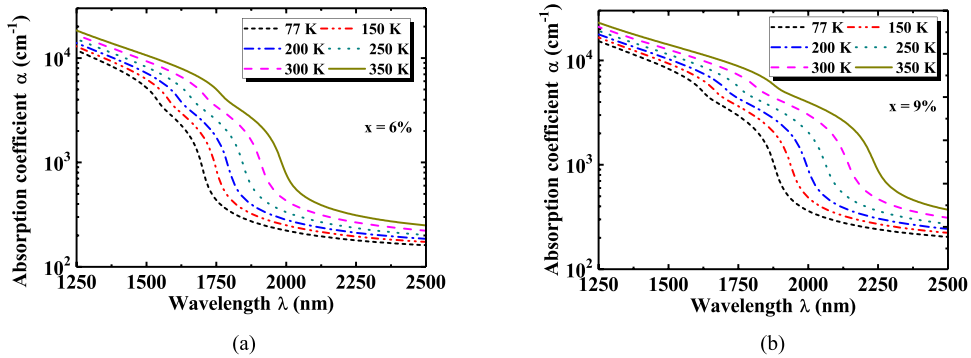

Fig. 8. Calculated absorption coefficient spectra for pseudomorphic $Ge_{1-x}Sn_x$ on Ge with (a) x = 6% and (b) x = 9% at different temperatures.

demonstrate that f_T increases with increasing collector current, and maximal f_T value is obtained around ~ 0.7 mA. The maximum value of f_T is controlled by the peripheral carrier contribution, leading to a significant reduction in the emitter resistance because of τ_{RC} decreases. Thus, f_T increases with the collector current value. The results also show that, at lower collector current values, f_T increases linearly with the collector current as the junction capacitance decreases with DC supply. For higher values of the collector current ($I_{Cop} > 0.1$ mA), f_T tends to saturate because the intrinsic carrier conductance decreases. As a result, the capacitance charging time (τ_{RC}) becomes smaller than the forward transit time.

4.4 Effect of Temperature on the Cut-off Frequency

In this section, we discuss the impact of temperature on the f_T and total time delay of GeSn HPTs for the fixed emitter and base-layer doping concentrations of $N_E = 1 \times 10^{19} \text{cm}^{-3}$ and $N_B = 1 \times 10^{18} \text{cm}^{-3}$, respectively (Fig. 7). The results show that τ_{Total} increases with temperature, leading to a significant decrease in the f_T because the base transit time ($\tau_b = t_b^2/2D_p$) and τ_{RC} ($\tau_{RC} = r_e C_{ECop}$) are strongly dependent on the temperature. However, the base-collector transit time ($\tau_{bc} = t_{bc}/2V_s$) decreases with increasing temperature. With increasing temperature, the parasitic and depletion capacitances decrease. However, small-signal emitter resistance increases drastically (r_e is proportional to T, as shown in Eq. 1), resulting in an increase in τ_{RC}. In contrast, the minority hole D_p decreases exponentially with temperature, thereby increasing τ_b. The rise in temperature causes a decrease in the base-collector space charge region (t_{bc}) because τ_{bc} decreases. The magnitude of $\tau_b + \tau_{RC} \gg \tau_{bc}$ increases τ_{Total} at higher temperatures. Fig. 8 shows
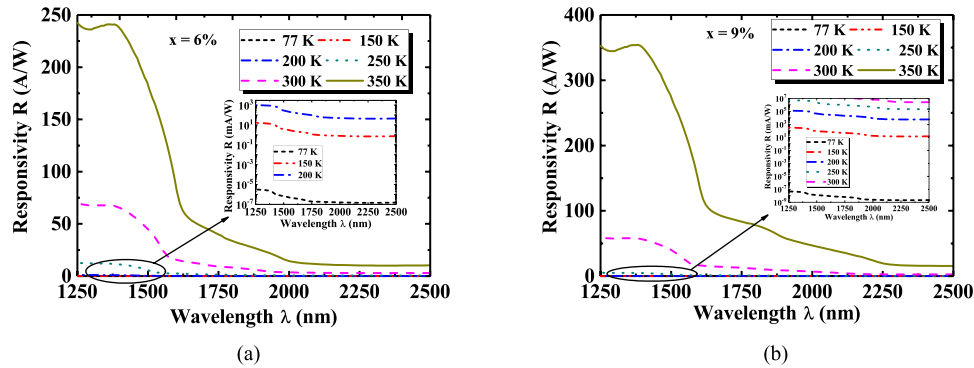
Fig. 9. Calculated SR for *p-n-p* GeSn HPT with (a) x = 6% and (b) x = 9% at different temperatures. The inset shows the variation of SR with incident wavelength at 77, 150, 200, and 250 K, respectively.

the calculated f_T value for the GeSn HPT, which can exceed 51 GHz at low temperatures ($\sim 25\,K$) and 44 GHz at temperatures up to $\sim 373.15\,K$. With an increase in temperature from 25 K to 373 K, total transit time (τ_{Total}) increases by 14.32% and f_T decreases by 13.72%. Therefore, GeSn HPTs are a potential candidate for high-speed applications.

4.5 Effect of Temperature on the Absorption Coefficient and Responsivity

In this section, we study the impact of temperature on the absorption coefficient spectra and SR. Fig. 8 shows the calculated absorption coefficient spectra at different temperatures for pseudo-morphic GeSn on Ge with Sn concentrations of 6% and 9%. The results demonstrate that the absorption coefficient increases with temperature because of the reduced bandgap at higher temperatures. As a result, the joint density-of-states, which is proportional to $\sqrt{\hbar\omega - E_g}$, becomes larger at higher temperatures and increases the absorption coefficient. The absorption coefficient also increases with increasing Sn concentrations because of the bandgap reduction caused by Sn-alloying. Therefore, a high absorption coefficient and high efficiency in the MIR wavelength can be obtained by increasing the Sn content in the $Ge_{1-x}Sn_x$ base layer. The calculated SR at different temperatures is shown in Fig. 9 for the GeSn base layer with Sn concentrations of 6% and 9%. As the temperature increases, SR increases, because of the increase in the small-signal current gain. Furthermore, as the Sn concentration increases in the base layer, the photodetection cut-off wavelength shifts to 1920 nm for x = 6% and 2220 nm for x = 9% at 300 K, which is caused by the direct bandgap shrinkage with Sn-alloying. As shown in Fig. 9, there is a strong temperature dependence of SR for the HPT detector; the responsivity value increases by more than 5.7 times (1550 nm) and 3.6 times (2500 nm) for x = 6%, and 9.17 times (1550 nm) and 6.05 times (2500 nm) for x = 9% of the magnitude, when the temperature increased from 300 K to 350 K. As a result, the direct bandgap energy decreases (Eq. 12), leading to a significant increase in the small-signal current gain. Therefore, SR increases with temperature and Sn concentrations. These results suggest that the proposed GeSn HPT can achieve higher performance at higher temperatures and thus is suitable for uncooled applications.

4.6 Effect of Temperature on the Noise Components and SNR

We also present the effect of temperature and frequency on the noise behavior and SNR of GeSn HPTs with optimized doping concentrations in various layers and input resistance (R_i) of 10 kΩ. The impact of temperature on the noise characteristics and SNR at the output of the device is shown in fig. 10. The calculated result shows that all the noise components increase with an increase in operating temperature. However, the rate of increase of shot noise at the B-E junction and
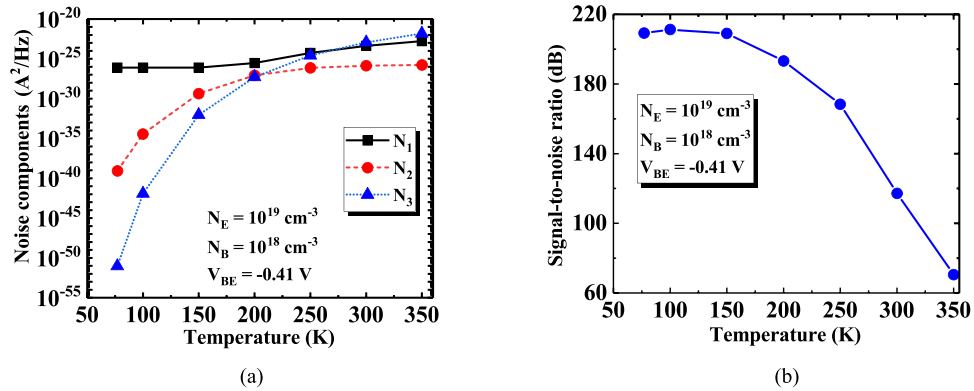
Fig. 10. Variations in (a) various noise components, and (b) SNR with the temperature at the output of the detector.
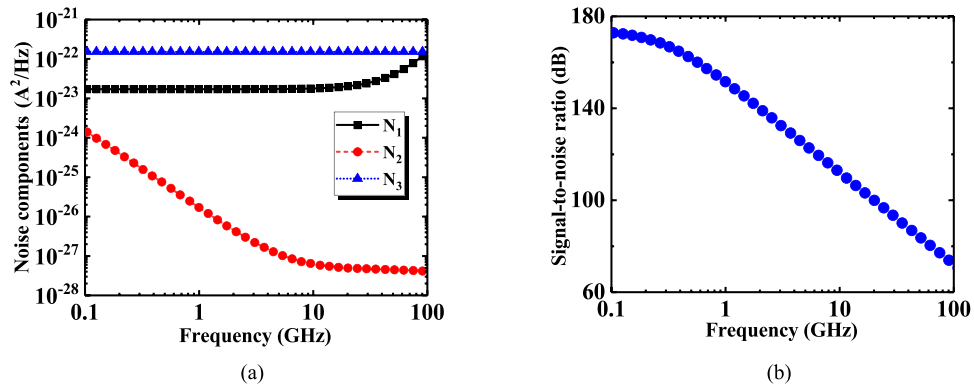

Fig. 11. Variations in (a) various noise components, and (b) SNR with operating frequency.

thermal noise is more than the rate of increase of the shot noise at the B-C junction. For the lower operating temperatures (up to 275 K), shot noise at the B-C junction dominates (the magnitude is higher than the thermal noise and shot noise at the B-E junction), but beyond 275 K, thermal noise starts dominating (the magnitude becomes larger). The increase in various noise components with increasing temperature is due to the transconductance (g_{mop}) under illumination (g_{mop} increases with operating temperature). The rise in temperature increases the gain of the device [44] because the collector current under illumination (I_{cop}) increases, leading to increase in the transconductance ($g_{mop} = I_{cop}/V_T$) and mean square value of shot noise current component at B-C junction. Thermal noise is directly proportional to the temperature ($\overline{v_{rop}^2} = 4kTR_{bop}f_T$) and square of g_{mop} (given in Eq. 11). Hence, with an increase in temperature, the noise components increase. Variation of SNR with temperature is shown in fig. 10(b). SNR decreases with an increase in temperature. This is expected as we consider the variation of various noise components with temperature. Next, the variation of various noise components and SNR with operating frequency is shown in Fig. 11. The results show that the thermal noise (N_3) is independent of frequency. Shot noise at the B-E junction at different temperatures initially decreases at frequencies of up to 10 GHz; however, it becomes nearly constant at further frequencies up to 100 GHz. Shot noise at the B-C junction initially remains nearly constant with frequencies of up to 30 GHz; however, it starts increasing quickly beyond 30 GHz. This behavior can be explained by the small-signal current gain (β), which decreases at the frequency of 30 GHz due to the RC and the parasitic effect. SNR is approximately

TABLE 2

Comparison Between f_T Values of the Proposed Structure and The Existing HPTs

Reference	Cut-off Frequency, f_T (GHz)	Response time (ps)	SNR (dB)
Milano et al. [34]	20	-	50
Khan et al. [45]	7.5	7.38	-
Ma et al. [43]	21.29	-	-
Tegegne et al. [46]	30	5.9	-
Quan et al. [47]	-	-	58
Dupont et al. [48]	-	--	77
This Work	57	$\sim$3.4	$\sim$117

constant up to 1 GHz; beyond 1 GHz, it starts decreasing rapidly with frequency because of the shot noise at the B-C junction, which starts to dominate beyond 1 GHz. The SNR estimated for the GeSn HPT can exceed 200 dB at 77 K and 60 dB at 350 K in operating frequency ranges up to 100 GHz. Thus, the proposed GeSn HPT is a suitable candidate for high-speed, low-noise photodetection.

4.6 Performance Comparison Between Our Proposed Device and Existing Devices

A comparison between the various values, such as f_T, response time, and SNR, obtained from our designed device and the existing phototransistors is given in Table 2. The GeSn-based HPT shows a higher value of f_T and SNR and lower response time than the existing phototransistors, which verifies that the proposed device can be a suitable detector for high-speed MIR applications.

5. Conclusion

We investigated the impacts of temperature and the doping of emitter and base layers on the characteristics of GeSn HPTs, including transit time, f_T, f_{max}, and SR, to achieve high-performance photodetection in the 2–3-μm wavelength range. The calculated noise components and SNR as a function of temperature at the output of the HPT showed that the GeSn HPT can provide much larger f_T to achieve high speed and responsivity at longer wavelengths. In addition, the GeSn HPT showed extremely high SNR, responsivity, and f_T above a low-bias voltage of 0.4 V. The f_T increases with emitter doping, whereas it decreases with base doping and temperature. With the incorporation of Sn in the $Ge_{1-x}Sn_x$ base, responsivity and f_T significantly increased due to the increase in the cut-off wavelength and mobility. The GeSn HPT showed higher responsivity at higher temperatures due to an increase in the absorption coefficient and current gain. However, the SNR decreases at higher temperatures due to the increase in various noise components. The f_T and f_{max} were calculated as $\sim$57 GHz and 145 GHz at room temperature with optimized emitter and base-layer doping concentrations of $N_E = 1 \times 10^{19} cm^{-3}$ and N_B of $1 \times 10^{18} cm^{-3}$, respectively. Extremely high responsivity, SNR, low response time, and CMOS compatibility of the GeSn HPT on the Si substrate pave the way for future high-speed uncooled MIR photodetection for a wide range of applications.

Acknowledgment

References

[1] R. A. Yotter and D. M. Wilson, "A review of photodetectors for sensing light-emitting reporters in biological systems," *IEEE Sens. J.*, vol. 3, no. 3, pp. 288–303, Jun. 2003.

[2] M. Long *et al.*, "Room temperature high-detectivity mid-infrared photodetectors based on black arsenic phosphorus," *Sci. Adv.*, vol. 3, no. 6, pp. 1–7, 2017.

[3] M. N. Abedin, T. F. Refaat, O. V. Sulima, and U. N. Singh, "AlGaAsSb-InGaAsSb HPTs with high optical gain and wide dynamic range," *IEEE Trans. Electron Devices*, vol. 51, no. 12, pp. 2013–2018, 2004.

[4] S. Dupont, M. Fendler, F. Jorge, J.-P. Vilcot, and D. Decoster, "Signal to noise ratio enhancement using heterojunction bipolar phototransistor by base current compensation," in *Proc. Int. Topical Meeting Microw. Photon.*, 2000, pp. 59–61.

[5] H. Shao, W. Li, A. Torfi, D. Moscicka, and W. I. Wang, "Room-temperature p-n-p AlGaAsSb-InGaAsSb heterojunction phototransistors with cutoff wavelength at 2.55 μm," *IEEE Photon. Technol. Lett.*, vol. 18, no. 22, pp. 2326–2328, Nov. 2006.

[6] N. Chand, P. A. Houston, and P. N. Robson, "Gain of a heterojunction bipolar phototransistor," *IEEE Trans. Electron Devices*, vol. 32, no. 3, pp. 622–627, Mar. 1985.

[7] X. Zhou, J. S. Ng, and C. H. Tan, "InAs photodiode for low temperature sensing," *Sensors, Syst., Next-Gener. Satellites XIX*, vol. 9639, 2015, Art. no. 96390V-(1-7).

[8] R. A. Miller, H. So, T. A. Heuser, and D. G. Senesky, "High-temperature Ultraviolet Photodetectors: A Review.," 2018, a*rXiv:1809.07396v1*.

[9] O. Esame, Y. Gurbuz, I. Tekin, and A. Bozkurt, "Performance comparison of state-of-the-art heterojunction bipolar devices (HBT) based on AlGaAs/GaAs, Si/SiGe and InGaAs/InP," *Microelectronics J.*, vol. 35, no. 11, pp. 901–908, 2004.

[10] E. Kasper, M. Kittler, M. Oehme, and T. Arguirov, "Germanium tin: silicon photonics toward the mid-infrared [Invited]," *Photon. Res.*, vol. 1, no. 2, pp. 69–76, 2013.

[11] J. D. Sau and M. L. Cohen, "Possibility of increased mobility in Ge-Sn alloy system," *Phys. Rev. B - Condens. Matter Mater. Phys.*, vol. 75, no. 4, pp. 1–7, 2007.

[12] B. Mukhopadhyay, G. Sen, R. Basu, S. Mukhopadhyay, and P. K. Basu, "Prediction of large enhancement of electron mobility in direct gap Ge1−xSnxAlloy," *Phys. Status Solidi Basic Res.*, vol. 254, no. 11, pp. 1–7, 2017.

[13] S. Gupta, Y.-C. Huang, Y. Kim, E. Sanchez, and K. C. Saraswat, "Hole mobility enhancement in compressively strained Ge0.93Sn0.07 pMOSFETs," *IEEE Electron Device Lett.*, vol. 34, no. 7, pp. 831–833, Jul. 2013.

[14] M. Zhao, L. Liu, J. Wang, R. Liang, L. Xiao, and J. Xu, "Enhanced hole mobility of Ge/GeSn pMOSFETs with a GeSnO interface layer and a NiGe Schottky source/drain," in *Proc. Device Res. Conf. Digest*, 2014, vol. 377, no. 2006, pp. 93–94.

[15] G. Han *et al.*, "High-mobility germanium-tin (GeSn) P-channel MOSFETs featuring metallic source/drain and sub-370°C process modules," in *Proc. Techn. Digest - Int. Electron Devices Meeting*, 2011, no. 2010, pp. 402–404.

[16] Y. C. Fang, K. Y. Chen, C. H. Hsieh, C. C. Su, and Y. H. Wu, "N-MOSFETs formed on solid phase epitaxially grown GeSn film with passivation by oxygen plasma featuring high mobility," *ACS Appl. Mater. Interfaces*, vol. 7, no. 48, pp. 26374–26380, 2015.

[17] T. H. Liu *et al.*, "High-mobility GeSn n-channel MOSFETs by low-temperature chemical vapor deposition and microwave annealing," *IEEE Electron Device Lett.*, vol. 39, no. 4, pp. 468–471, 2018.

[18] H. Tran *et al.*, "Systematic study of Ge1-xSnx absorption coefficient and refractive index for the device applications of Si-based optoelectronics," *J. Appl. Phys.*, vol. 119, no. 10, 2016, Art. no. 103106.

[19] H. Lan and C. W. Liu, "Band alignments at strained Ge 1 − x Sn x / relaxed Ge 1 − y Sn y heterointerfaces," *J. Appl. Phys. D Appl. Phys.*, vol. 50, 2017, Art. no. 13LT02.

[20] B. Dutt *et al.*, "Theoretical analysis of GeSn alloys as a gain medium for a si-compatible laser," *IEEE J. Sel. Top. Quantum Electron.*, vol. 19, no. 5, Sep.-Oct. 2013, Art. no. 1502706.

[21] M. Oehme, K. Kostecki, M. Schmid, F. Oliveira, E. Kasper, and J. Schulze, "Epitaxial growth of strained and unstrained GeSn alloys up to 25% Sn," *Thin Solid Films*, vol. 557, pp. 169–172, 2014.

[22] J. Zheng *et al.*, "Growth of high-Sn content (28%) GeSn alloy films by sputtering epitaxy," *J. Cryst. Growth*, vol. 492, pp. 29–34, 2018.

[23] M. Oehme *et al.*, "GeSn p-i-n detectors integrated on Si with up to 4% Sn," *Appl. Phys. Lett.*, vol. 101, no. 14, pp. 1–5, 2012.

[24] Y. Dong *et al.*, "Germanium-Tin on Si avalanche photodiode: Device design and technology demonstration," *IEEE Trans. Electron Devices*, vol. 62, no. 1, pp. 128–135, Jan. 2015.

[25] J. Mathews, R. Roucka, J. Xie, S. Q. Yu, J. Meńdez, and J. Kouvetakis, "Extended performance GeSn/Si(100) p-i-n photodetectors for full spectral range telecommunication applications," *Appl. Phys. Lett.*, vol. 95, no. 13, 2009, Art. no. 133506.

[26] H. H. Tseng *et al.*, "GeSn-based p-i-n photodiodes with strained active layer on a Si wafer," *Appl. Phys. Lett.*, vol. 103, no. 23, 2013, Art. no. 1907.

[27] A. K. Pandey, R. Basu, and G. E. Chang, "Optimized Ge1-xSnx/Ge multiple-quantum-well heterojunction phototransistors for high-performance SWIR photodetection," *IEEE Sens. J.*, vol. 18, no. 14, pp. 5842–5852, Jul. 2018.

[28] H. Kumar and R. Basu, "Noise analysis of group IV material-based heterojunction phototransistor for fiber-optic telecommunication networks," *IEEE Sens. J.*, vol. 18, no. 22, pp. 9180–9187, Nov. 2018.

[29] G. E. Chang, R. Basu, B. Mukhopadhyay, and P. K. Basu, "Design and modeling of GeSn-based heterojunction phototransistors for communication applications," *IEEE J. Sel. Topics Quantum Electron.*, vol. 22, no. 6, Nov.-Dec. 2016, Art. no. 8200409.

[30] R. Basu and H. Kumar, "Noise analysis of optimized Ge/Ge1−xSnx/Ge p–n–p heterojunction phototransistors for long-wavelength optical receivers," *Opt. Quantum Electron.*, vol. 51, no. 2, pp. 1–12, 2019.

[31] W. Wang *et al.*, "Floating-base germanium-tin heterojunction phototransistor for high-efficiency photodetection in short-wave infrared range," *Opt. Express*, vol. 25, no. 16, pp. 10170–10173, 2017.

[32] W.-T. Hung, D. Barshilia, R. Basu, H. H. Cheng, and G.-E. Chang, "Silicon-based high-responsivity GeSn short-wave infrared heterojunction phototransistors with a floating base," *Opt. Lett.*, vol. 45, no. 5, pp. 1088–1091, 2020.

[33] Y. S. Wang *et al.*, "High-speed InGaAs P-I-N photodetector with planar buried heterostructure," *IEEE Trans. Electron Devices*, vol. 56, no. 6, pp. 1347–1350, Jun. 2009.

[34] R. A. Milano, P. D. Dapkus, and G. E. Stillman, "An analysis of the performance of heterojunction phototransistors for fiber optic communications," *IEEE Trans. Electron Devices*, vol. 29, no. 2, pp. 266–274, Feb. 1982.

[35] W. Wang, Q. Zhou, Y. Dong, E. S. Tok, and Y.-C. Yeo, "Critical thickness for strain relaxation of Ge$_{1-x}$Sn$_x$ ($x \leq 0.17$) grown by molecular beam epitaxy on Ge(001)," *Appl. Phys. Lett.*, vol. 106, no. 23, 2015, Art. no. 232106.

[36] A. Gassenq *et al.*, "Raman spectral shift versus strain and composition in GeSn layers with 6%-15% Sn content," *Appl. Phys. Lett.*, vol. 110, no. 11, 2017, Art. no. 112101.

[37] G. Ottaviani, C. Canali, F. Nava, and J. W. Mayer, "Hole drift velocity in high-purity Ge between 8 and 220°K," *J. Appl. Phys.*, vol. 44, no. 6, pp. 2917–2918, 1973.

[38] Y.P. Varshni, "Temperature dependence of the energy gap in semiconductors," *Physica*, vol. 34, no. 1, pp. 149–154, 1967.

[39] R. Quay, C. Moglestue, V. Palankovski, and S. Selberherr, "A temperature dependent model for the saturation velocity in semiconductor materials," *Mater. Sci. Semicond. Process.*, vol. 3, no. 1–2, pp. 149–155, 2000.

[40] H. Kumar and R. Basu, "Effect of active layer scaling on the performance of Ge$_{1-x}$Sn$_x$ phototransistors," *IEEE Trans. Electron Devices*, vol. 66, no. 9, pp. 3867–3873, Sep. 2019.

[41] H. Kumar, R. Basu, and J. Gupta, "Small-signal compact circuit modeling of group IV material-based heterojunction phototransistors for optoelectronic receivers," *IEEE Trans. Electron Devices*, vol. 66, no. 4, pp. 1797–1803, Apr. 2019.

[42] A. K. Pandey, R. Basu, H. Kumar, and G. E. Chang, "Comprehensive analysis and optimal design of Ge/GeSn/Ge p-n-p infrared heterojunction phototransistors," *IEEE J. Electron Devices Soc.*, vol. 7, no. 1, pp. 118–126, 2019,.

[43] P. Ma *et al.*,"Influence of base structural parameters on responsivity and characteristic frequency of SiGe heterojunction phototransistor," in *Proc. 14th IEEE Int. Conf. Solid-State Integr. Circuit Technol.*, 2018, pp. 1–3.

[44] H. Wang and G. I. Ng, "Electrical properties and transport mechanisms of InP/InGaAS HBTs operated at low temperature," *IEEE Trans. Electron Devices*, vol. 48, no. 8, pp. 1492–1497, Aug. 2001.

[45] H. A. Khan, A. A. Rezazadeh, and Y. Zhang, "Photoresponse modeling and analysis of InGaP/GaAs double-HPTs," *IEEE J. Quantum Electron.*, vol. 50, no. 12, pp. 1044–1051, Dec. 2014.

[46] Z. G. Tegegne, C. Viana, J. L. Polleux, M. Grzeskowiak, and E. Richalot, "Study of lateral scaling impact on the frequency performance of SiGe heterojunction bipolar phototransistor," *IEEE J. Quantum Electron.*, vol. 54, no. 3, Jun. 2018, Art. no. 4600109.

[47] Q. Zhou, S. X. Guo, Z. H. Li, J. Y. Song, and Y. C. Chang, "Analysis of responsivity and signal-to-noise ratio in PEPT," *Chin. Phys. Lett.*, vol. 29, no. 11, pp. 9–12, 2012.

[48] S. Dupont, M. Fendler, F. Jorge, and D. Decoster, "Signal-to-noise ratio enhancement using heterojunction bipolar phototransistor by base current compensation," in *Proc. Int. Topical Meeting Microw. Photon.*, 2000, pp. 59–61.